Delft University of Technology

Tuning electron transfer by crystal facet engineering of BiVO$_4$ for boosting visible-light driven photocatalytic reduction of bromate

Liu, Guoshuai; Zhu, Yukun; Yan, Qun; Wang, Han; Wu, Peng; Shen, Yaoliang; Doekhi-Bennani, Yasmina

Important note
To cite this publication, please use the final published version (if applicable).
Please check the document version above.

3

Tuning Electron Transfer by Crystal Facet Engineering of BiVO₄ for Boosting

4

Visible-Light Driven Photocatalytic Reduction of Bromate

5

6

7   Guoshuai Liu[a‡], Yukun Zhu[b‡], Qun Yan[a,c,*], Han Wang[a], Peng Wu[c], Yaoliang Shen[c], and Yasmina

8   Doekhi-Bennani[d]

9

10   [a] *School of Environmental and Civil Engineering, Jiangnan University, Wuxi 214122, China*

11   [b] *School of Environmental Science and Engineering, State Key Laboratory of Bio-fibers and*

12   *Eco-textiles, Qingdao University, Qingdao 266071, China*

13   [c] *Jiangsu Collaborative Innovation Center of Technology and Material of Water Treatment, Suzhou*

14   *215011, China*

15   [d] *Department of Water Management, Section Sanitary Engineering, Delft University of Technology,*

16   *PO Box 5048, 2600 GA Delft, The Netherlands*

17   [‡] *The authors contribute equally to this work.*

18

19

20   **Corresponding author:**

21   * Qun Yan

22   School of Environmental and Civil Engineering, Jiangnan University, Wuxi 214122, China.

23   E–mail: yanqun@jiangnan.edu.cn (Q. Yan).

24
25
26
27

ABSTRACT：

Removal of bromate (BrO_3^-) has gained increasing attention in drinking water treatment process. Photocatalysis technology is an effective strategy for bromate removal. During the photocatalytic reduction of bromate process, the photo-generated electrons are reductive species toward bromate reduction and photo-generated holes responsible for water oxidation. In this study, the monoclinic bismuth vanadate ($BiVO_4$) single crystal was developed as a visible photocatalyst for the effective removal of bromate. The as-synthesized $BiVO_4$ photocatalyst with optimized {010} and {110} facets ratio could achieve almost 100% removal efficiency of BrO_3^- driven by visible light with a first-order kinetic constant of 0.0368 min^{-1}. As demonstrated by the electron scavenger experiment and density functional theory (DFT) calculations, the exposed facets of $BiVO_4$ should account for the high photocatalytic reduction efficiency. Under visible light illumination, the photo-generated electron and holes were spatially transferred to {010} facets and {110} facets, respectively. The $BiVO_4$ single crystal photocatalyst may serve as an attractive photocatalyst by virtue of its response to the visible light, spatially charge transfer and separation as well as high photocatalytic activity, which will make the removal of BrO_3^- in water much easier, more economical and more sustainable.

Keywords: bromate; bismuth vanadate; photocatalysis; crystal engineering

INTRODUCTION

Bromate (BrO_3^-) originated from the chlorination or ozonation process in bromide-containing water has attracted the attention of many researchers (Bouland et al., 2005; Chen et al., 2016; Parker et al., 2014, Zhu et al.,). The drinking water standard of BrO_3^- in the European Union and the U.S. Environmental Protection Agency is less than 10 μg/L (Shen et al., 2017; Weinberg et al., 2003; Wu et al., 2013). To overcome this obstacle, considerable progress has been made regarding the transformation of BrO_3^- to Br^- by using various technologies, such as electrochemical reductive treatment (Xie and Shang, 2007), zero-valent iron (Wang et al., 2009; Zhang et al., 2015) and FeOOH catalytic reduction (Nie et al., 2014). Although these already established technologies can remove BrO_3^- effectively, they may suffer from various problems such as high cost, operational complexity, as well as the potential secondary pollution risk induced by metal leaching (Ayoubi-Feiz et al., 2015; Lin et al., 2016; Noguchi et al., 2003).

Recently, photocatalysis process was regarded as a superior technology to remove BrO_3^- (Noguchi et al., 2002). Compared with the conventional removal methods mentioned above, photocatalysis shows fascinating potential for bromate removal systems due to its high efficiency, low-cost and environmental benignity (Ayoubi-Feiz et al., 2015; Lin et al., 2016; Noguchi et al., 2003). As the widely used photocatalyst, TiO_2 based photocatalysts had been extensively employed in bromate removal by UV-light driven photocatalysis, whereas the efficient conversion of BrO_3^- to Br^- was contributed to the photo-generated electrons at conduction band (CB) (Li et al., 2016; Liu et al., 2016; Zhang et al., 2005).

However, the photocatalytic systems based on TiO_2-photocatalysis still suffer from some problems for bromate removal: (i) The wide bandgap (E_g = 3.2 eV) of TiO_2 can only be responsively under UV light irradiation (UV, 3% ratio of solar light). This may cause inconvenience in practical applications (Perry et al., 2009; Williams et al., 2008; Yang et al., 2020a; Yang et al., 2020b). (ii) The reducing agent in the photocatalytic system is photo-generated electrons. It is important to improve the

quantum efficiency of photoelectrons to participate in the bromate reduction reaction (Pan and Zhu, 2010; Wang et al., 2020a; Yang et al., 2019; Zhu et al., 2020c; Wang et al., 2020b; Wang et al., 2019). (iii) As a redox couple in the reaction depends on generated-electrons and holes, the photocatalytic reduction half-reaction is interdependent to the oxidation half-reaction mediated by photo-generated holes at the valence band (VB). Therefore, there is a growing interest in developing high overall efficiency visible light driving photocatalysts (Zhang et al., 2019; Zhu et al., 2019; Zhu et al., 2020a).

In the BrO_3^- reduction system, BrO_3^- acts as an electron acceptor, and the reduction reaction (1 e^- process) is not considered as a limiting step for the overall photocatalytic redox reaction. On the other hand, the oxidation of water (4 e^- process) is observed as a bottleneck or the rate-determining step (Zhu et al., 2020b). Based on the above-mentioned points, the premise for effective BrO_3^- reduction is to find a visible photocatalyst with high reductive activity, high selectivity and water oxidation ability.

Monoclinic $BiVO_4$ has been widely used in photocatalysis or photoelectrochemical process for the water oxidation to produce oxygen due to its efficient and active visible light photocatalytic properties (Nakabayashi et al., 2017; Saison et al., 2015). Therefore, the oxidation reaction would not hamper the reductive half-reaction (bromate reduction reaction). On the premise that $BiVO_4$ can efficiently oxidize water, the major water oxidation products are oxygen rather than hydroxyl radicals (Nakabayashi et al., 2017; Saison et al., 2015). This can mitigate the problem of the re-oxidation of bromine ions by hydroxyl radicals. Recent associated studies on the preparation of single crystal $BiVO_4$ photocatalysts have shown that photo-generated carriers could be transferred to different exposed crystal facets (Li et al., 2013; Zhu et al., 2017), the reduction and oxidation reactions were spatially separated with a high reaction extent. Learned from these experiences, the reduction surface (photo-generated electron rich surface) of $BiVO_4$ can be made by the crystal facet engineering, thus improving the quantum efficiency of photo-generated electrons involved in the

102   bromate reduction reaction.

103   Herein, three kinds of BiVO$_4$ crystals (BVO-a, b and c) with different exposed facets were

104   prepared and applied to the photocatalytic reduction of bromate under visible light. Additionally, the

105   structure and morphology of BiVO$_4$ single crystals were characterized using X-ray diffraction (XRD)

106   and field emission scanning electron microscopy (FESEM). Furthermore, the BrO$_3^-$ reduction

107   performance was evaluated by calculating the conversion of BrO$_3^-$ to Br$^-$. Lastly, the optical

108   properties and electron configuration were estimated using density functional theory (DFT), and the

109   bandgap, band position, and effective electron mass were also taken into consideration. The possible

110   photocatalytic reduction mechanisms of BrO$_3^-$ by BiVO$_4$ crystals were proposed.

EXPERIMENTAL SECTION

112   **Synthesis of the photocatalyst.** BiVO$_4$ powders were prepared by liquid-solid state reaction. 5

113   mmol of V$_2$O$_5$ and 10 mmol of Bi(NO$_3$)$_3$·5H$_2$O were added in 60 mL of DI water. The precursor

114   solution was stirred until a yellow solution was formed. The pH of the solution was regulated to 1.0,

115   0.5 and 0.1 by ammonia solution or dilute nitric acid solution, and then the solution was vigorously

116   stirred at room temperature for 5 days. The obtained BiVO$_4$ powder was separated by centrifugation,

117   washed with DI water and dried at 60 °C. Moreover, the obtained BiVO$_4$ powders synthesized at

118   different pH values of 1.0, 0.5 and 0.1 were labeled as BiVO$_4$-a, BiVO$_4$-b and BiVO$_4$-c.

119   **Characterization.** The powder X-ray diffraction (XRD) characterization was conducted on an

120   X-ray diffractometer (Bruker D8 Adv., Germany). The crystalline phase and morphology of the

121   as-prepared BiVO$_4$ samples were characterized by an X-ray diffractometer (Bruker D8 Adv.,

122   Germany) and afield emission scanning electron microscope (FESEM, Type-4800, Hitachi, Japan),

123   respectively. A spectrophotometer (Type-UV2550, Shimadzu, Japan) recorded the UV−vis diffuse

124   reflectance spectroscopy (DRS) of the powders. The photoelectrochemical measurements were

125   conducted using a CHI760E electrochemical workstation. The photocurrent measurements were

126   carried out under visible light irradiation (300 W Xenon lamp).

127   **Theoretical Calculations.** The optimization of the unit cell of monoclinic scheelite $BiVO_4$ was

128   performed using the CASTEP code with the projector augmented wave (PAW) pseudopotentials (Liu

129   et al., 2017), and the parameter was set according to the reference (Long et al., 2008). The angle b of

130   monoclinic scheelite $BiVO_4$ was set to 134.9° for simplification, the detailed parameters can be

131   found in Table S1. The stable crystal configuration of the bulk and the cleavage surface with the

132   optimized lowest energy are shown in Figure S1.

133   **Experimental Setup and Procedures.** The BrO_3^- ions removal performance was tested according

134   to the previous method reported by our team (Liu et al., 2019). Both BrO_3^- and Br^- ions were

135   determined by an ion chromatograph analyzer (LC-10A, Shimadzu, Japan).

136   **RESULTS AND DISCUSSION**

137   **Characterization of BiVO₄ Photocatalysts.** The XRD patterns of three types of as-synthesized

138    $BiVO_4$ photocatalysts are presented in Figure 1A. All diffraction patterns of samples ($BiVO_4$-a, b and

139   c) showed sharp diffraction peaks and all typical peaks were attributed to monoclinic scheelite

140    $BiVO_4$ crystal phase (JCPDS No. 14-0688, space group: $C2/c$), evidently suggesting that the $BiVO_4$

141   photocatalysts have high crystallinity (Liu et al., 2014). Considering the phenomenon that the (121)

142   peak was the highest peak for separated $BiVO_4$-a, b and c, the (121) peak was selected as the

143   benchmark to evaluate the possible exposed surface in $BiVO_4$ crystal qualitatively, i.e., the intensity

144   ratios of the diffraction peak of (040) and (110) compared with (121). The intensityof (040)

145   diffraction peak followed the order of $BiVO_4$-a > $BiVO_4$-b > $BiVO_4$-c, while that of (110) diffraction

146   peak showed a reverse order, i.e., $BiVO_4$-c > $BiVO_4$-b > $BiVO_4$-a. However, the intensity of (110)

147   diffraction peak of $BiVO_4$-c was stronger than that of $BiVO_4$-b and a ($BiVO_4$-c > $BiVO_4$-b >

148    $BiVO_4$-a). According to Wang's study, this intensity difference in XRD pattern indicated that the

149   (040) diffraction peak was the dominant peak for $BiVO_4$-a, and that for $BiVO_4$-c was (110) (Wang et

150   al., 2011). The FESEM image of $BiVO_4$-a exhibited a sheet-like geometry with a length of 1.5 μm,

151   width of 400-nm, and thickness of 150-nm, respectively (Figure 1B). The $BiVO_4$-b sample exhibited

152 a polyhedral box shape (Figure 1C) with an average size of about 1.5 μm. In addition, the $BiVO_4$-c

153 with an octahedral shape of about 2 μ m was observed in Figure1D. To further identify the exposed

154 crystal faces, the corresponding HRTEM image for $BiVO_4$-a is given in Figure 1E.

155 The corresponding selected area electron diffraction (SAED) pattern in Figure 1F (inset picture) is

156 taken from the sheet-like $BiVO_4$-a sample (Figure 1E), revealing the growth orientation in

157 accordance with the results of XRD measurements. As determined by XRD result, and with different

158 b axis orientations for different sheets, the d spacings measured from SAED (zone axis [010]) were

159 2.61 Å, which agreed well with the lattice spacings of (200) monoclinic $BiVO_4$ (Wang et al., 2011).

160 The growth direction was along the (040) facet, i.e., {010} crystal planes; therefore, the sheet-like

161 $BiVO_4$-a growed along the b axis as seen in the HRTEM images (Figure 1F). Based on these

162 analyses and calculations, a simple schematic illustration of the exposed crystal surface is presented

163 in the insets in Figure 1B, C and D according to the XRD and HRTEM analysis. The XPS spectra of

164 Bi 4f, V 2p and O 1s are illustrated in Figure S2. The Bi 4f consisted of two peaks at the binding

165 energy of 156.3 and 161.5 eV, while the V 2p spectra showed two peaks of 514.0 eV and 521.7 eV,

166 respectively. Moreover, the O 1s spectra was detected at the binding energy of 527.1 eV.

167

168 **<u>Figure 1 (A-F)</u>**

169

170 **Photocatalytic Reduction of BrO_3^- by $BiVO_4$ Photocatalysts.** The feasibility of photocatalytic

171 reduction of BrO_3^- using $BiVO_4$ photocatalysts under visible light irradiation irradiation were

172 examined by photocatalytic experiment. No BrO_3^- reduction was observed in the absence of

173 photocatalysts, which excluded the direct visible light driven photolysis of BrO_3^- reduction. As

174 illustrated in Figure 2A, the concentration of BrO_3^- decreased from initial 1000 to 0 μg L^{-1} (below

175 the detection limit) for $BiVO_4$-b after 150 minutes of reaction, which exhibited almost 100% BrO_3^-

176 removal efficiency. However, $BiVO_4$-a and $BiVO_4$-c reduced the initial BrO_3^- concentration (1000

177   μg L^{-1}) to 130 and 230 μg L^{-1}, respectively. The BrO$_3^-$ removal performance can be well indexed to

178   the first-order reaction k = 0.0368 min^{-1} for BiVO$_4$-b (Figure 2B), which was 2.08 and 3.94 times

179   higher than that of BiVO$_4$-a (0.0177 min^{-1}) and BiVO$_4$-c (0.0094 min^{-1}), respectively. (Table S2).

180   These results demonstrated that the BiVO$_4$-b sample showed superior photocatalytic bromate

181   removal performance than that of BiVO$_4$-a and -c samples which might be benefited from the facet

182   effect of BiVO$_4$ crystal. Moreover, the stability of the BiVO$_4$ photocatalysts was also evaluated and

183   the result can be seen in Figure S3. during the recycling process, the photocatalytic performance of

184   BiVO$_4$ was with high stability, amount to 3% activity loss after five-cycles. During the recycling

185   process, the photocatalytic performance of BiVO$_4$ was of high stability with the activity loss

186   amounting to 3% activity loss after five-cycles

187

188   **Figure 2 (A and B)**

189

190   **Mechanisms Insight.** To further understand the BrO$_3^-$ reduction mechanism by BiVO$_4$

191   photocatalyst, the electron scavenger experiments were implemented by adding S$_2$O$_8^{2-}$ (Romão et al.,

192   2015). As a typical electron scavenger, the degradation performance of BrO$_3^-$ was decreased

193   obviously after the introduction of S$_2$O$_8^{2-}$ (Figure S4 and Table S3). Notably, the bromate removal

194   nearly disappeared when 5 mmol of K$_2$S$_2$O$_8$ was added. Thus, it could be concluded that the

195   photo-generated electrons were the reactive species during the BrO$_3^-$ photocatalytic reduction

196   process.

197   As we know, for semiconductor photocatalysis, the optical properties are directly related to the

198   intrinsic electron configuration and thus influence the photocatalytic performance. Figure 3A shows

199   the DRS spectra of BiVO$_4$ samples with different exposed surfaces. The adsorption properties of the

200   obtained three types of BiVO$_4$ were all typical visible light-driven photocatalysts with an absorption

201   edge at approximately 536 nm (E_g = 2.31 eV), which was in line with the previous report (Su et al.,

202   2011). The DFT calculation regarding optical properties was conducted to better understand the

203   relationship of light absorption with exposed surface. As shown in Figure 3B, there was no obvious

204   difference in the absorption threshold for polycrystal, {010} and {110} facets BiVO$_4$, respectively,

205   which was in accordance with the DRS results. Based on the above DRS and DFT calculation results,

206   it can be concluded that the optical properties of BiVO$_4$ samples may not be the major reasons for the

207   great difference in the photocatalytic removal of bromate.

208

209   **Figure 3 (A and B)**

210

$$E_{\text{VB}} = \chi - E^e + \frac{E_{\text{g}}}{2} \tag{1}$$

211

$$E_{\text{CB}} = E_{\text{VB}} - E_{\text{g}} \tag{2}$$

212

213   Furthermore, the theoretical positions of energy band position of BiVO$_4$ at pH = pH$_{\text{pzc}}$ were

214   calculated using the following conventional eqn. 1 and 2 (Xu and Schoonen, 2000). E_{e} is the free

215   electron energy (4.5 V), E_{g} is the measured band gap. By substituting these absolute

216   electronegativities of Bi, V and O to eqn. 1 and 2, the E_{VB} of 2.80 V and E_{CB} of 0.49 V (SHE) were

217   obtained (Cooper et al., 2014). Although the valence band position of BiVO$_4$ was suitable for

218   hydroxyl radicals generation, according to the previous literature, BiVO$_4$ was generally considered as

219   a highly efficient photocatalyst for water oxidation to produce oxygen rather than hydroxyl radicals,

220   thus making the reduction of BrO$_3^-$ more efficient towards Br$^-$ conversion (Nakabayashi et al., 2017;

221   Saison et al., 2015).

222   As shown in Figure S1, VO$_4^{3-}$ was a stretched tetrahedron. In the stretched BiO$_8$ dodecahedron, Bi

223   atoms were surrounded by 8 O atoms, and the four bond lengths were different (2.467, 2.466, 2.471,

224   and 2.528 Å) (Stoltzfus et al., 2007; Yang et al., 2013). As we know, the dipole moments played an

225   important role in photocatalysis, especially on the effective separation of carriers. A big dipole

226 moment always means a high driving force makes efficient photo-generated carriers transfer (Li et al.,

227 2014). In this regard, the absolute numerical value of dipole moment is calculated to be 0.79 and

228 0.68 D on {010} and {110} facets, respectively. The larger dipole moment of the BiO polyhedrons

229 for {010} facet demonstrates greater distortion of the {110} surface layer, hence leading to a larger

230 internal polarization which is conducive to the charge separation and higher activity for the

231 photocatalytic reduction of BrO_3^-.

232

233 **Table 1**

234

235   To further understand the electronic configuration of the two exposed crystal facets, the band

236 structure of $BiVO_4$ is plotted in Figure 4A. Considering the symmetry of the monoclinic system, the

237 path selected from the Brillouin zone was along Z → G→ Y → A → B → D → E → C. The DFT

238 calculated E_g for $BiVO_4$ was 2.12 eV, close to the experimental value (2.31 eV). The highest band

239 energy level and lowest energy level were located at different K-points, which indicated the typical

240 indirect band gap property. Furthermore, we can calculate the effective carrier masses of {010} and

241 {110} facets based on the curvatures of the bands in the corresponding directions by fitting parabolic

242 functions to the conduction band minimum (CBM) and valence band maximum (VBM) of $BiVO_4$.

243 According to the Eq. (3) (Li et al., 2014), the effective electron masses can be estimated, where k is

244 the wave vector, and E_k is the energy corresponding to the wave vector k.

245
$$m^* = \pm h^2 (\frac{d^2 E_k}{dk^2})^{-1} \tag{3}$$

246 The calculated results are summarized in Table 1.The effective electron masses were approximately

247 0.13 m_0 and 0.30 m_0, and the effective hole masses are estimated to be approximately 0.18 m_0 and

248 0.57 m_0 for {010} and {110} surfaces, respectively. In the photocatalytic process, lower effective

249 mass means higher drift velocity, and the photo-generated hole/electron pairs could be transfered to

250 the surface of photocatalyst (Li et al., 2014). Therefore, the effective electron mass of {010} was

10

251    $0.13\ m_0$, obviously lower than that of {110} facets making it favorable for the photocatalytic bromate

252   reduction process.

253

254   **<u>Figure 4 (A and B)</u>**

255

256   According to the dipole moment and charge transport calculation, the presence of {010} facet

257   exposed $BiVO_4$ was beneficial for the charge separation. As revealed from the photocurrent of

258    $BiVO_4$-a, $BiVO_4$-b and $BiVO_4$-c in Figure 4B, $BiVO_4$-b possessed a much higher photocurrent than

259    $BiVO_4$-a and $BiVO_4$-c. The intense photocurrent generally means a higher hole/electron pairs

260   separation efficiency (Li et al.). As shown in Figure 4B, the $BiVO_4$-b sample with {010} facet

261   exposed maintained a high separation efficiency of hole/electron pairs, which was in well agreement

262   with the result of dipole moment calculations.

263   The intrinsic reason for the separation of photo-generated carriers on the {010} and {110} of

264    $BiVO_4$ crystal facets was evaluated by the DFT calculation method (Pan et al., 2011). Figure 5A

265   shows the density of states (DOS) calculation results (where Fermi energy was set as 0 eV).We can

266   ascertain the conduction band edge and valence band edge from Figure 5A, where the conduction

267   band edge for {110} facets was 1.33 eV, and that for {010} was 2.15 eV. Thus, the energy differences

268   for conduction bands (Δ_{CB}) between {010} and {110} facets was about 0.82 eV. Similarly, we could

269   calculate the Δ_{VB} by analyzing the DOS curves and the result is about 0.20 eV between {010} and

270   {110} facets. The existed difference well demonstrated that the transfer trend of photo-generated

271   electron was from {110} to {010} facets in the thermodynamic view. Within this context, the

272   electrons were accumulated on {010} facets, whereas the holes were enriched on {110} facets. Based

273   on the calculated results obtained in Figure 5A, the schematic diagram of spatial photo-generated

274   carriers separation between {110} and {010} facets is schematic shown in Figure 5B. Furthermore,

275   the Work function (W) calculation results are shown in Figure 5C and 5D. The W of {010} and {110}

276 facets was 6.2 eV and 4.5 eV, respectively. The W value of {010} facets is obvious bigger than that

277 of {110} facets, which makes the {010} facets have a higher electron capture ability (Gao et al.,

278 2011). The results were in line with the density of state (DOS) analysis, where the photo-generated

279 electrons were separated spatially with the photo-generated holes during photocatalytic process to

280 form electron-rich {010} facets and hole-rich {110} facets.

281

282 **<u>Figure 5 (A, B, C and D)</u>**

283

284 For a practical photocatalytic reaction, reduction reactions were accompanied by oxidation

285 reactions. To achieve a high photocatalytic efficiency (in this study, is photocatalytic reduction of

286 bromate), high oxidation reactions involved by photo-generated holes must be considered. To

287 clarify the mechanism deeply, the test of $BiVO_4$ photocatalyst utilized in water oxidation under

288 visible light irradiation of O_2 evolution with BrO_3^- as electron sacrificial agent ($NaBrO_3$, 0.1 mol L^{-1})

289 was conducted, and the photocatalytic O_2 evolution performance is shown in Table S4. As shown in

290 Table S4, the $BiVO_4$-b exhibited the highest oxygen production with the rate of 11.70 μmol h^{-1}, and

291 the order of oxygen production rate was $BiVO_4$-b (11.70 μmol h^{-1}) >> $BiVO_4$-a (2.30 μmol h^{-1}) >

292 $BiVO_4$-c (1.50 μmol h^{-1}). The results evidently confirmed that the $BiVO_4$-b showed the highest water

293 oxidation, as an overall reaction, the photo-reduction performance was correlated with the oxidation

294 ability. Therefore, the $BiVO_4$-b sample with an optimized exposure ratio of the {010} and {110}

295 surfaces exhibited the highest photocatalytic bromate reduction activity. The conceivable intrinsic

296 mechanisms are schematically showed in Figure 6. Under the irradiation of visible light,

297 photo-generated carriers were separated toward different surfaces for the polyhedral box shape

298 $BiVO_4$ photocatalyst, i.e., the photo-generated electrons (thermodynamic potential of 0.49 V, SHE)

299 and photo-generated holes (2.80 V, SHE) were transferred to different facets of $BiVO_4$ crystal. As

300 shown in Figure 6, the {010} facets were the electron-rich surfaces, whereas the holes were

accumulated on the {110} surfaces. The electron with a redox potential of 0.49 V was a robust

reductive for bromate reduction ($BrO_3^- + 6H^+ + 6e^- \rightarrow Br^- + 3H_2O$, $E^\circ = 1.423$ V). And

photo-generated hole with a high redox potential of 2.80 V could decompose H_2O to produce oxygen

efficiently ($2H_2O - 4e^- \rightarrow O_2 + 4H^+$, $E^\circ = 1.23$ V). In this manner, BrO_3^- could be regarded as the

electron acceptor and *in-situ* reduced at {010} facets, while the water oxidation reaction was

occurred at {110} surfaces to produce O_2. The photo-generated electron-hole pairs were spatially

separated, and the oxidation and reduction reactions occurred at different crystal facets; thus, a high

bromate reduction efficiency and selectivity on $BiVO_4$ single crystal with optimized {010} and {110}

ratio could be achieved. Besides, a systemic comparison with conventional photocatalyst of TiO_2,

traditional bulk $BiVO_4$ or Bi_2MoO_6 documented from literatureis summarized in Table S5. The

$BiVO_4$-b sample with active exposed facets ratio could remove almost 100% of BrO_3^-, whose kinetic

constant was significantly higher than that of other conventional photocatalysts.

<u>Figure 6</u>

 Conclusions. To achieve efficient removal of BrO_3^-, we herein developed single crystal

photocatalysts $BiVO_4$ with different exposed facets. The {010} facets are exposed electron-rich

surfaces with a higher dipole moment and a lower effective masse of electrons/holes, which is more

favorable for the photocatalytic bromate reduction reaction. Under visible light illumination, the

photo-generated reductive electrons and oxidative photo-generated holes are spatially transported to

{010} and {110} facets, respectively. During the bromate photocatalytic removal process, water acts

as an electron donor, thus avoiding the risk of secondary pollution, making the BrO_3^- removal of

high efficiency. This investigation provides a simple and effective strategy for enhanced degradation

of bromate without complicated preparation procedure, which makes the bromate removal more

efficient and sustainable, and also gives a guideline for the development of single crystal

326 photocatalyst for bromate photocatalytic reduction.

REFERENCES

333 Ayoubi-Feiz B, Aber S, Sheydaei M. Effect of oxidants on photoelectrocatalytic decolourization using
334   α-Fe$_2$O$_3$/TiO$_2$/activated charcoal plate nanocomposite under visible light. RSC Adv. 2015; 5: 19368-19378.

335 Bouland S, Duguet J-P, Montiel A. Evaluation of bromate ions level introduced by sodium hypochlorite during
336   post-disinfection of drinking water. Environ. Technol. 2005; 26: 121-126.

337 Chen F, Yang Q, Zhong Y, An H, Zhao J, Xie T, et al. Photo-reduction of bromate in drinking water by metallic Ag and
338   reduced graphene oxide (RGO) jointly modified BiVO$_4$ under visible light irradiation. Water Res. 2016; 101:
339   555-563.

340 Cooper JK, Gul S, Toma FM, Le C, Glans PA, Guo J, et al. Electronic structure of monoclinic BiVO$_4$. Chem. Mater. 2014;
341   26: 5365-5373.

342 Gao E, Wang W, Shang M, Xu J. Synthesis and enhanced photocatalytic performance of graphene-Bi$_2$WO$_6$ composite.
343   Phys. Chem. Chem. Phys. 2011; 13: 2887-2893.

344 Li R, Zhang F, Wang D, Yang J, Li M, Zhu J, et al. Spatial separation of photogenerated electrons and holes among {010}
345   and {110} crystal facets of BiVO$_4$. Nat. Commun. 2013; 4: 1432-1439.

346 Li X, Pi Y, Xia Q, Li Z, Xiao J. TiO$_2$ encapsulated in Salicylaldehyde-NH$_2$-MIL-101 (Cr) for enhanced visible
347   light-driven photodegradation of MB. Appl. Catal. B-Environ. 2016; 191: 192-201.

348 Li Y, Jiang Y, Ruan Z, Lin K, Yu Z, Zheng Z, et al. Simulation-guided synthesis of graphitic carbon nitride beads with 3D
349   interconnected and continuous meso/macropore channels for enhanced light absorption and photo-catalytic
350   performance. J. Mater. Chem. A. 2017; 5: 21300-21312.

351 Li Z, Dai Y, Ma X, Zhu Y, Baibiao H. Tuning photocatalytic performance of the near-infrared-driven photocatalyst
352   Cu$_2$(OH)PO$_4$ based on effective mass and dipole moment. Phys. Chem. Chem. Phys. 2014; 16: 3267-3273.

353 Lin K-YA, Lin C-H, Chen S-Y, Yang H. Enhanced photocatalytic reduction of concentrated bromate in the presence of
354   alcohols. Chem. Eng. J. 2016; 303: 596-603.

355 Liu G, Liu S, Lu Q, Sun H, Xu F, Zhao G. Synthesis of monoclinic BiVO$_4$ microribbons by sol-gel combined with
356   electrospinning process and photocatalytic degradation performances. J. Sol-gel Sci. Techn. 2014; 70: 24-32.

357 Liu G, You S, Ma M, Huang H, Ren N. Removal of nitrate by photocatalytic denitrification using nonlinear optical
358   material. Environ. Sci. Technol. 2016; 50: 11218-11225.

359 Liu G, You S, Tan Y, Ren N. In situ photochemical activation of sulfate for enhanced degradation of organic pollutants in
360   water. Environ. Sci. Technol. 2017; 51: 2339-2346.

361 Liu G, You S, Zhang Y, Huang H, Spanjers H. Conjugated donor-acceptor (D-A) supramolecule catalyst for
362   visible-light-driven photocatalytic removal of bromate in water. J. Colloid Interf. Sci. 2019; 553: 666-673.

363 Long M, Cai W, Kisch H. Visible light induced photoelectrochemical properties of n-BiVO$_4$ and n-BiVO$_4$/p-Co$_3$O$_4$. J.

364   Phys. Chem. C 2008; 112: 548-554.

365 Nakabayashi Y, Nishikawa M, Saito N, Terashima C, Fujishima A. Significance of hydroxyl radical in photoinduced
366   oxygen evolution in water on monoclinic bismuth vanadate. J. Phys. Chem. C 2017; 121: 25624-25631.

367 Nie Y, Hu C, Li N, Yang L, Qu J. Inhibition of bromate formation by surface reduction in catalytic ozonation of organic
368   pollutants over β-FeOOH/Al$_2$O$_3$. Appl. Catal. B-Environ. 2014; 147: 287-292.

369 Noguchi H, Nakajima A, Watanabe T, Hashimoto K. Removal of bromate ion from water using TiO$_2$ and alumina-loaded
370   TiO$_2$ photocatalysts. Water Sci. Technol. 2002; 46: 27-31.

371 Noguchi H, Nakajima A, Watanabe T, Hashimoto K. Design of a photocatalyst for bromate decomposition: Surface
372   modification of TiO$_2$ by pseudo-boehmite. Environ. Sci. Technol. 2003; 37: 153-157.

373 Pan C, Zhu Y. New type of BiPO$_4$ oxy-acid salt photocatalyst with high photocatalytic activity on degradation of dye.
374   Environ. Sci. Technol. 2010; 44: 5570-5574.

375 Pan J, Liu G, Lu GQ, Cheng HM. On the true photoreactivity order of {001}, {010}, and {101} facets of anatase TiO$_2$
376   crystals. Angew. Chem. Int. Edit. 2011; 50: 2133.

377 Parker KM, Zeng T, Harkness J, Vengosh A, Mitch WA. Enhanced formation of disinfection byproducts in shale gas
378   wastewater-impacted drinking water supplies. Environ. Sci. Technol. 2014; 48: 11161-9.

379 Perry Iv JJ, Perman JA, Zaworotko MJ. Design and synthesis of metal–organic frameworks using metal–organic
380   polyhedra as supermolecular building blocks. Chem. Soc. Rev. 2009; 38: 1400-1417.

381 Romão JS, Hamdy MS, Mul G, Baltrusaitis J. Photocatalytic decomposition of cortisone acetate in aqueous solution. J.
382   Hazard. Mater. 2015; 282: 208-215.

383 Saison T, Chemin N, Chanéac C, Durupthy O, Mariey L, Maugé Fo, et al. New insights into BiVO$_4$ properties as visible
384   light photocatalyst. J. Phys. Chem. C 2015; 119: 12967-12977.

385 Shen W, Lin F, Jiang X, Li H, Ai Z, Zhang L. Efficient removal of bromate with core-shell Fe@Fe$_2$O$_3$ nanowires. Chem.
386   Eng. J. 2017; 308: 880-888.

387 Stoltzfus MW, Woodward PM, Ram S, Jae-Hyun K, Bruce B. Structure and bonding in SnWO$_4$, PbWO$_4$, and BiVO$_4$:
388   lone pairs vs inert pairs. Inorg. Chem. 2007; 46: 3839-50.

389 Su J, Guo L, Bao N, Grimes CA. Nanostructured WO$_3$/BiVO$_4$ Heterojunction films for efficient photoelectrochemical
390   water splitting. Nano Lett. 2011; 11: 1928-1933.

391 Wang D, Jiang H, Zong X, Xu Q, Ma Y, Li G, et al. Crystal facet dependence of water oxidation on BiVO$_4$ sheets under
392   visible light irradiation. Chem. Eur. J. 2011; 17: 1275-1282.

393 Wang Q, Snyder S, Kim J, Choi H. Aqueous ethanol modified nanoscale zerovalent iron in bromate reduction: synthesis,
394   characterization, and reactivity. Environ. Sci. Technol. 2009; 43: 3292-3299.

395 Wang W, Han Q, Zhu Z, Zhang L, Zhong S, Liu B. Enhanced photocatalytic degradation performance of organic
396   contaminants by heterojunction photocatalyst BiVO$_4$/TiO$_2$/RGO and its compatibility on four different
397   tetracycline antibiotics. Adv. Powder Technol. 2019; 30: 1882-1896.

398 Wang Y, Ding K, Xu R, Yu D, Wang W, Gao P, et al. Fabrication of BiVO$_4$/BiPO$_4$/GO composite photocatalytic material
399   for the visible light-driven degradation. J. Clean. Prod. 2020a; 247: 119108.

400 Wang Y, Yu D, Wang W, Gao P, Zhong S, Zhang L, et al. Synthesizing Co$_3$O$_4$-BiVO$_4$/g-C$_3$N$_4$ heterojunction composites
401   for superior photocatalytic redox activity. Sep. Purif. Technol. 2020b; 239: 116562.

402 Weinberg HS, Delcomyn CA, Unnam V. Bromate in chlorinated drinking waters: occurrence and implications for future
403   regulation. Environ. Sci. Technol. 2003; 37: 3104-3110.

404 Williams G, Seger B, Kamat PV. TiO$_2$-graphene nanocomposites. UV-assisted photocatalytic reduction of graphene oxide.
405   ACS Nano 2008; 2: 1487-1491.

406 Wu X, Yang Q, Xu D, Zhong Y, Luo K, Li X, et al. Simultaneous adsorption/reduction of bromate by nanoscale
407   zerovalent iron supported on modified activated carbon. Ind. Eng. Chem. Res. 2013; 52: 12574-12581.

408 Xie L, Shang C. The effects of operational parameters and common anions on the reactivity of zero-valent iron in
409   bromate reduction. Chemosphere 2007; 66: 1652-1659.

410 Xu Y, Schoonen MAA. The absolute Energy position of conduction and valence bands of selected semiconducting
411   minerals. Am. Mineral. 2000; 85: 543-556.

412 Yang J, Wang D, Zhou X, Li C. A theoretical study on the mechanism of photocatalytic oxygen evolution on BiVO$_4$ in
413   aqueous solution. Chem. Eur. J. 2013; 19: 1320-1326.

414 Yang R, Dong F, You X, Liu M, Zhong S, Zhang L, et al. Facile synthesis and characterization of interface charge
415   transfer heterojunction of Bi$_2$MoO$_6$ modified by Ag/AgCl photosensitive material with enhanced photocatalytic
416   activity. Mater. Lett. 2019; 252: 272-276.

417 Yang R, Zhong S, Zhang L, Liu B. PW12/CN@ Bi$_2$WO$_6$ composite photocatalyst prepared based on organic-inorganic
418   hybrid system for removing pollutants in water. Sep. Purif. Technol. 2020a; 235: 116270.

419 Yang R, Zhu Z, Hu C, Zhong S, Zhang L, Liu B, et al. One-step preparation (3D/2D/2D) BiVO$_4$/FeVO$_4$@rGO
420   heterojunction composite photocatalyst for the removal of tetracycline and hexavalent chromium ions in water.
421   Chem. Eng. J. 2020b; 390: 124522.

422 Zhang F, Jin R, Chen J, Shao C, Gao W, Li L, et al. High photocatalytic activity and selectivity for nitrogen in nitrate
423   reduction on Ag/TiO$_2$ catalyst with fine silver clusters. J. Catal. 2005; 232: 424-431.

424 Zhang H, Yu D, Wang W, Gao P, Zhang L, Zhong S, et al. Construction of a novel BON-Br-AgBr heterojunction
425   photocatalysts as a direct Z-scheme system for efficient visible photocatalytic activity. Appl. Surf. Sci. 2019;
426   497: 143820.

427 Zhang Y, Jing S, Liu H. Reactivity and mechanism of bromate reduction from aqueous solution using Zn–Fe(II)–Al
428   layered double hydroxides. Chem. Eng. J. 2015; 266: 21-27.

429 Zhu J, Pang S, Dittrich T, Gao Y, Nie W, Cui J, et al. Visualizing the nano cocatalyst aligned electric fields on single
430   photocatalyst particles. Nano Lett. 2017; 17: 6735-6741.

431 Zhu Y, Li J, Dong C, Ren J, Huang Y, Zhao D, et al. Red phosphorus decorated and doped TiO$_2$ nanofibers for efficient
432   photocatalytic hydrogen evolution from pure water. Appl. Catal. B-Environ. 2019; 255: 117764.

433 Zhu Y, Lv C, Yin Z, Ren J, Yang D. A [001]- Oriented hittorf's phosphorus nanorods/polymeric carbon nitride
434   heterostructure for boosting wide- spectrum- responsive photocatalytic hydrogen evolution from pure water.
435   Angew. Chem. Int. Edi. 2020a; 59: 868-873.

436 Zhu Y, Ren J, Zhang X, Yang D. Elemental red phosphorus-based materials for photocatalytic water purification and
437   hydrogen production. Nanoscale 2020b, 12, 13297-13310

438 Zhu Z, Wang C, Liang L, Yu D, Sun J, Zhang L, et al. Synthesis of novel ternary photocatalyst
439   Ag$_3$PO$_4$/Bi$_2$WO$_6$/multi-walled carbon nanotubes and its enhanced visible-light photoactivity for
440   photodegradation of norfloxacin. J. Nanosci. Nano. 2020c; 20: 2247-2258.

Table List

Table 1 Summary of the effective masses

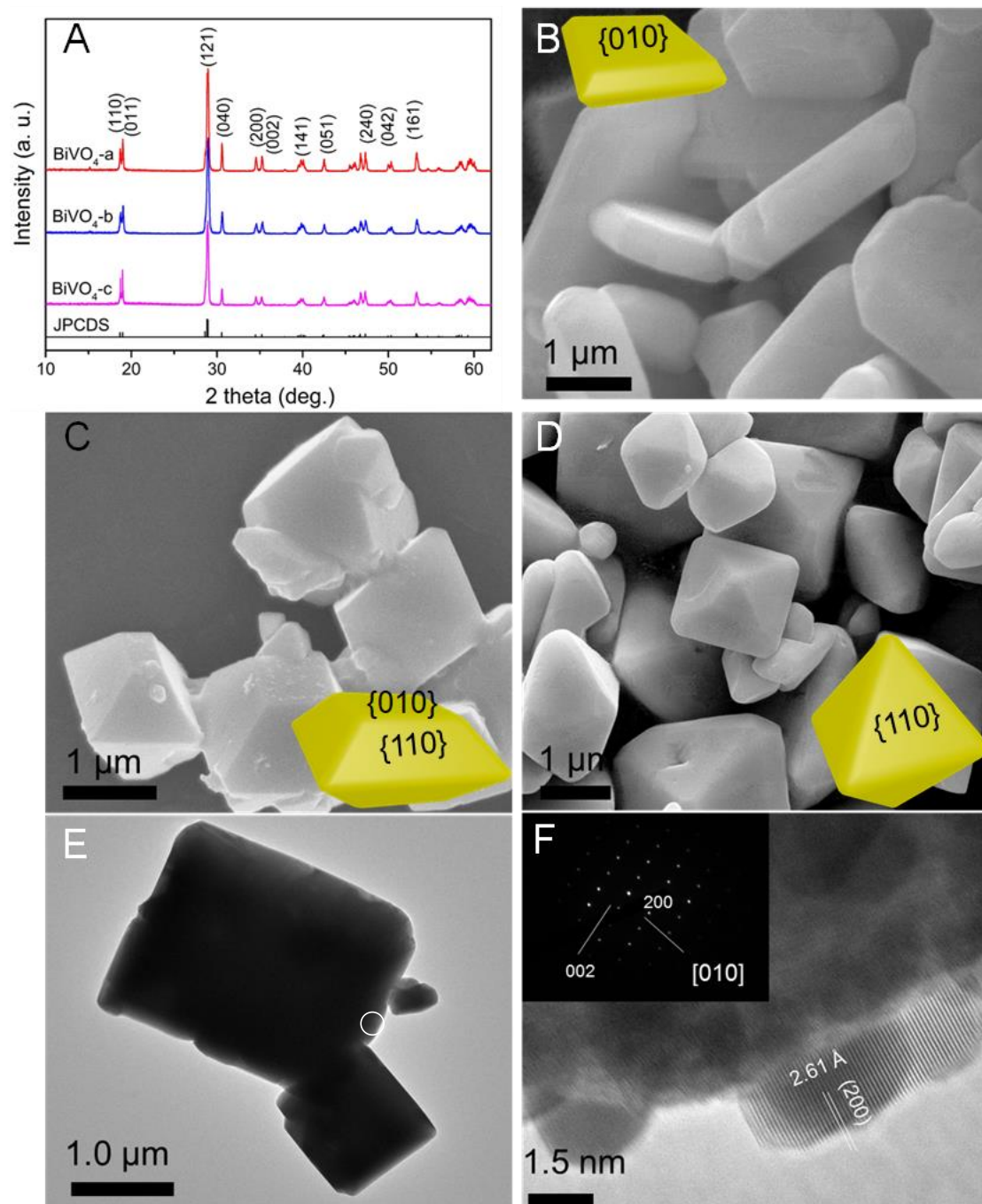|	{010}/m_0	{110}/m_0
m_h^*	0.18	0.57
m_e^*	0.13	0.30

Figure 1 XRD patterns of (A) BiVO$_4$ samples, SEM pictures of (B) BiVO$_4$-a, (C) BiVO$_4$-b, (D) BiVO$_4$-c, (E) TEM and HRTEM (F) pictures of BiVO$_4$-a.
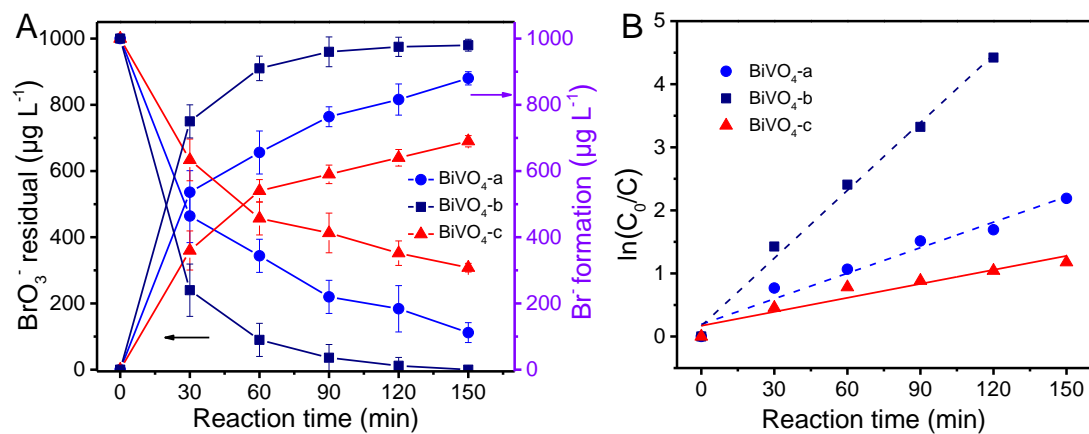
Figure 2 Time course of (A) photocatalytic reduction of BrO_3^- by $BiVO_4$ photocatalysts under visible light irradiation at pH 7.1 ± 0.4, (B) the corresponding kinetics rate constants derived from A.
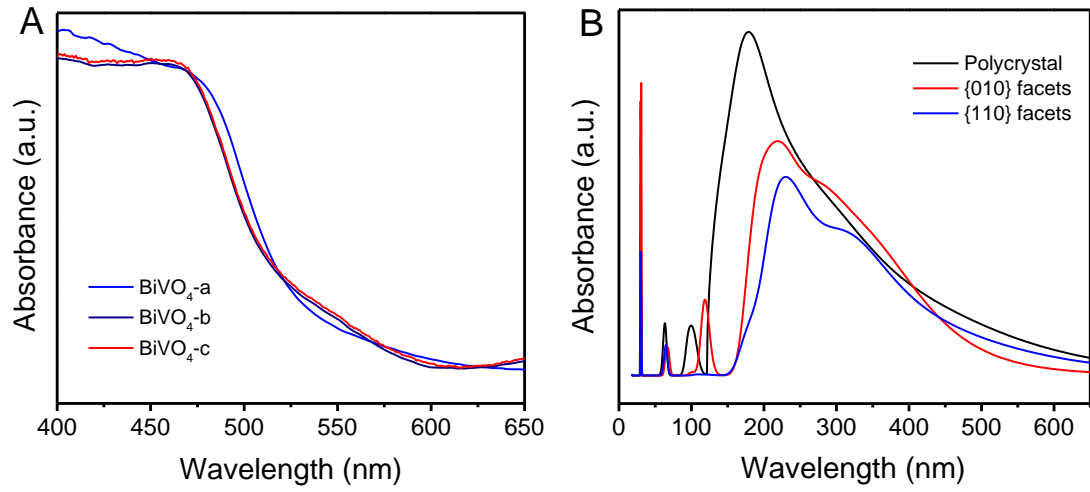
Figure 3 (A) The experimental diffuse reflectance spectra of BiVO$_4$ samples, (B) calculated absorption coefficient of polycrstal BiVO$_4$, {010} and {110} facets exposed BiVO$_4$.
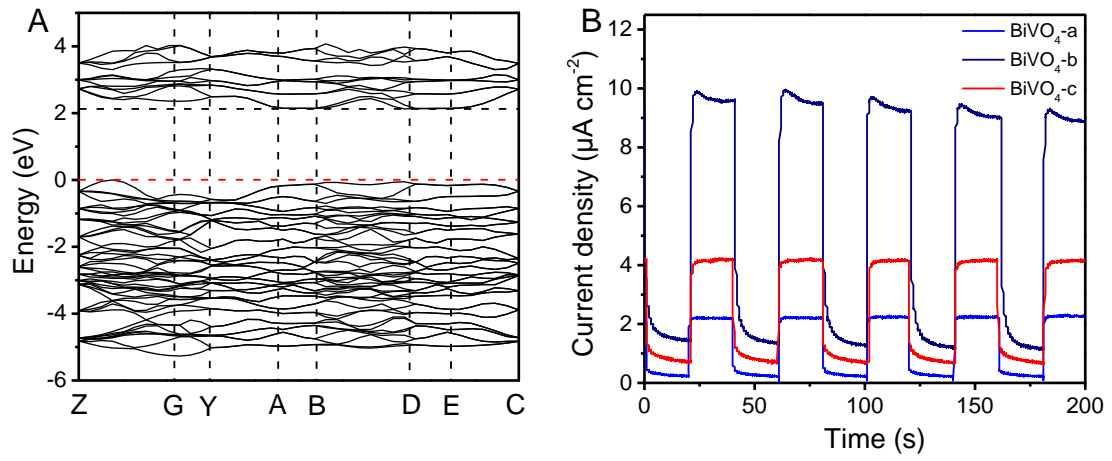
Figure 4 The band structure (A) of BiVO₄ crystal and (B) photocurrent-time curve of BiVO₄ samples.
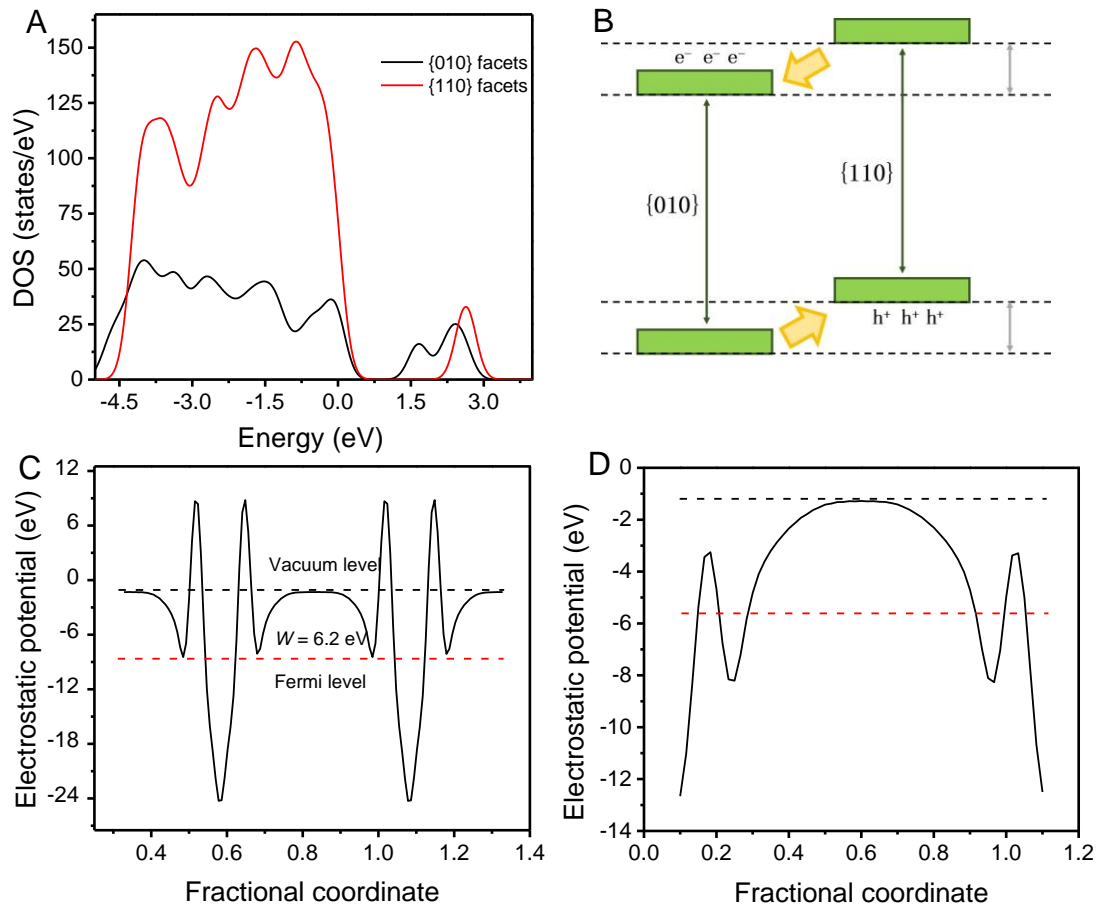
Figure 5 (A) The differences of the energy levels in conduction bands (Δ_{CB}) for {010} and {110} facets, (B) the scheme of carrier separation between {010} and {110} facets, (C) the workfunction (W) of {010} surface and (D) {110} surface.
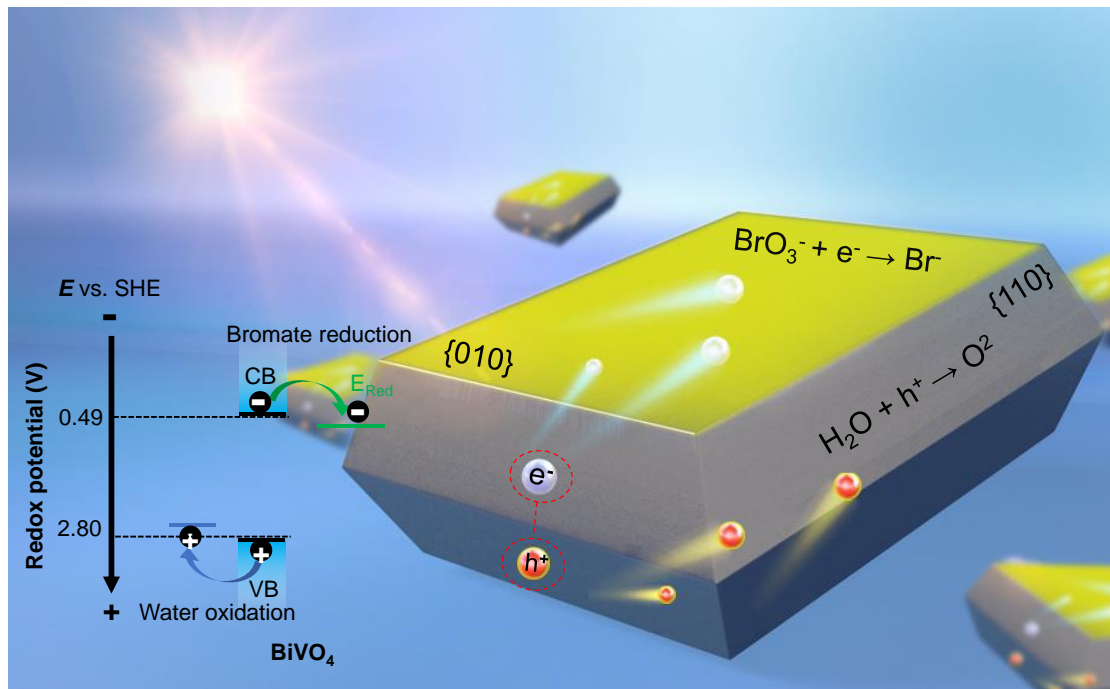
Figure 6 Schematic illustration of photocatalytic reduction of BrO_3^- by $BiVO_4$-b.